

1 **From slab to surface: Earthquake evidence for fluid migration at Uturuncu volcano, Bolivia**

2

3 Thomas S. Hudson^{a,*}, J-Michael Kendall^a, Matthew E. Pritchard^b, Jonathan D. Blundy^a,

4

Joachim H. Gottsmann^c

5

6 ^a *Department of Earth Sciences, University of Oxford, UK*

7

^b *Department of Earth and Atmospheric Sciences, Cornell University, USA*

8

^c *School of Earth Sciences, University of Bristol, UK*

9

10

11

Abstract

12

13 Uturuncu volcano is situated in the Bolivian Andes, directly above the world's largest crustal

14 body of silicic partial melt, the Altiplano-Puna Magma Body (APMB). Uturuncu last erupted

15 250,000 years ago, yet is seismically active and lies at the centre of a 70 km diameter uplifted

16 region. Here, we analyse seismicity from 2009 to 2012. Our earthquake locations, using a

17 newly developed velocity model, delineate the top and bottom of the APMB, reveal individual

18 faults, and reconcile differences in depth distribution between previous studies. Spatial

19 clustering analysis of these earthquakes reveals the orientations of the faults, which match

20 stress orientations from seismic anisotropy. Earthquake b-values derived from moment

21 magnitudes (1.4) differ significantly from those using local magnitude measurements (0.8).

22 We suggest that, if possible, moment magnitudes should always be used for accurate b-value

23 analysis. We interpret b-values > 1 in terms of fluid-enhanced seismicity. Shallow seismicity

24 local to Uturuncu yields b-values > 1.1 with some temporal variation, suggesting fluid

25 migration along pre-existing faults in a shallow hydrothermal system, likely driven by
26 advection from the APMB. Intriguingly, events deeper than the APMB also yield large b-values
27 (1.4), mapping the ascent into the lower crust of fluids originating from a subducting slab.
28 Cumulatively, these results provide a picture of an active magmatic system, where fluids are
29 exchanged across the more ductile APMB, feeding a shallow, fault-controlled hydrothermal
30 system. Such pathways of fluid ascent may influence our understanding of arc volcanism,
31 control future volcanic eruptions and promote the accumulation of shallow hydrothermal ore
32 deposits.

33

34

35

36

37

38

39

40

41

42

43

44

45

46

47

48

49 **1. Introduction**

50 Uturuncu is a volcano in the Bolivian Andes. It sits above the Altiplano-Puna Magma
51 (or Mush) Body (APMB), the world's largest zone of silicic partial melt (Pritchard et al., 2018).
52 The extent of the APMB has been imaged by ambient noise tomography and receiver
53 functions, suggesting a volume of 500,000 km³ of 20-30 % partial melt at 15 to 20 km below
54 sea-level (Chmielowski et al., 1999; Ward et al., 2013; Zandt et al., 2003). The APMB extent
55 has also been constrained by magnetotellurics, gravity and petrological methods (Comeau et
56 al., 2016; Schmitz et al., 1997). There is also evidence that melt may extend into the lower
57 crust (Kukarina et al., 2017). Although Uturuncu last erupted 250,000 years ago (Muir et al.,
58 2015), the volcano has been deforming for at least 50 years, at a rate of up to 1 cm/yr between
59 1992 and 2000 (Gottsmann et al., 2018; Henderson & Pritchard, 2017; Pritchard et al., 2018),
60 inviting the question of what is causing this inflation.

61

62 A number of seismological and other geophysical studies have recently focussed on
63 mapping the seismicity and imaging the crustal structure at Uturuncu. Both shallow and deep
64 crustal seismicity, above and below the APMB, have been observed (Jay, et al., 2012; Kukarina
65 et al., 2017; Sparks et al., 2008). Moment tensor analysis of this seismicity has shown both
66 double-couple (DC) shear earthquakes and earthquakes with a volumetric component
67 (Alvizuri & Tape, 2016). Seismic reveals a shallow stress field that mimics the orientations of
68 the faults associated with these earthquakes (predominantly NE-SW and NW-SE) (Maher &
69 Kendall, 2018). Analysis of local earthquake magnitudes suggests that b-values are
70 significantly less than one (0.66) (Hutchinson, 2015; Jay, et al., 2012; Maher & Kendall, 2018),
71 in stark contrast to studies of volcanic regions elsewhere (Greenfield et al., 2020; Murru et
72 al., 2007; Power et al., 1998; Wilks et al., 2017). The seismic velocity structure of the crust has

73 been constrained using receiver functions and ambient noise tomography (Chmielowski et
74 al., 1999; Ward et al., 2014; Zandt et al., 2003). This seismic velocity structure,
75 magnetotelluric (Comeau et al., 2016), and gravity (Del Potro et al., 2013) models image the
76 APMB and a high conductivity, low density and slow shear-velocity region extending vertically
77 from the APMB through the overlying upper crust.

78

79 Here we reanalyse seismic datasets recorded at Uturuncu between 2009 and 2010
80 and between 2010 and 2012, including a previously unstudied period in 2012. Previously,
81 earthquakes were detected and located using travel-time picks at individual stations. Here,
82 we use a method that combines energy from all stations simultaneously to improve the
83 detection threshold, picking accuracy and provide error estimates (Hudson et al., 2019; Smith
84 et al., 2020). Using this method, we detect more seismicity and map this seismicity with higher
85 accuracy than previous studies. Furthermore, we are able to address a depth discrepancy
86 between previous studies (see Pritchard et al., (2018)). Earthquake moment magnitudes are
87 calculated to reassess the relationship between the magnitude and total number of
88 earthquakes (i.e. b-value estimates and their temporal variations). We then use the more
89 accurately mapped seismicity combined with the b-value measurements to infer paths of fluid
90 migration through the crust at Uturuncu volcano.

91

92

93

94

95

96

97 **2. Methods**

98 Two seismometer networks were deployed over the period of 20th April 2009 to the
99 27th October 2012, with the ANDIVOLC network (Jay et al., 2012) (see gold inverted triangles,
100 Figure 1) operational until the 13th April 2010 and the PLUTONS network (Kukarina et al.,
101 2017) (see blue inverted triangles, Figure 1) operational for the remaining duration. The
102 ANDIVOLC network comprised of nine Mark Products L22 2 Hz seismometers and six Guralp
103 CMG-40T 30 s seismometers, all with Reftek RT130 dataloggers with a sampling rate of 50 Hz.
104 The PLUTONS network comprised of thirty-three Guralp CMG-3T 120 s seismometers, all with
105 Reftek RT130 dataloggers with a sampling rate of 100 Hz.

106

107 **2.1 Earthquake detection**

108 These instruments were used to detect the seismicity in Figure 1 using QuakeMigrate,
109 a microseismic detection algorithm (Hudson et al., 2019; Smith et al., 2020). The
110 QuakeMigrate method involves first band-pass filtering the data, before applying a Short-
111 Term-Average (STA) to Long-Term-Average (LTA) algorithm to each station and component
112 individually. We use the Z component for P phases and the N and E components for S phases.
113 These STA/LTA time series, henceforth referred to as onset functions, for each station are
114 then combined. These signals are migrated through time and space to search for a
115 coalescence of energy from the combination of peaks observed in the onset functions of
116 individual stations. If the coalescence of energy at a particular point in 3D space at a given
117 time is sufficiently high, then this triggers an event detection. The widths of the peaks in the
118 onset functions are approximated to be Gaussian, as in Drew et al. (2013), which provides a
119 measure of the temporal uncertainty associated with the P and S phase picks at individual
120 stations. This quantification of phase pick temporal uncertainty is a key strength of the

121 QuakeMigrate algorithm. We apply the QuakeMigrate algorithm to the Uturuncu seismic
122 dataset to obtain an initial catalogue of earthquakes, with P and S picks and their associated
123 uncertainties.

124

125 Once we have an initial catalogue, we relocate the events using the non-linear
126 relocation algorithm NonLinLoc (Lomax & Virieux, 2000), in order to obtain robust
127 hypocentral locations and uncertainties for the events. We then filter this catalogue by
128 physically meaningful parameters, such as the depth uncertainty, in order to minimise the
129 number of false detections in our catalogue. This also allows us to remove near surface events
130 that are located at shallow depths with anomalously high depth uncertainties compared to
131 the depth uncertainties of other shallow earthquakes, which are likely associated with mining
132 activity.

133

134 All parameters used in the QuakeMigrate earthquake detection and NonLinLoc
135 relocation processes are given in Supplementary Table S1. The band-pass filter values used
136 mean that our catalogue is comprised primarily of volcano-tectonic seismicity rather than
137 long-period and very-long-period seismicity. The velocity model used in the QuakeMigrate
138 migration is a 1D approximation of the 3D velocity tomography results (see Supplementary
139 Figure S1).

140

141 **2.2 Earthquake magnitudes**

142 The magnitude of an earthquake defines the size or energy of an earthquake. Broadly
143 there are two types of magnitude scale: relative magnitude scales, such as local magnitude,
144 M_L ; and absolute magnitude scales, such as moment magnitude, M_w (Hanks & Kanamori,

145 1979). Although local magnitudes are easier to measure, absolute magnitudes provide an
146 estimate of the actual moment or energy release of an earthquake rather an empirical
147 measure, and so allow for more robust analysis of general trends in number of earthquakes
148 vs. magnitude, as well as the underlying physical mechanisms generating the seismicity. We
149 therefore use the moment magnitude scale, but also calculate local magnitudes for reference.
150 Descriptions of the exact methods used to calculate M_w and M_L in this study are provided in
151 the Supplementary Material.

152

153 **2.4 Calculation of overall and temporal variations in b-value**

154 The Gutenberg-Richter distribution describes how usually there are many more
155 smaller earthquakes than larger earthquakes, and this trend follows a logarithmic relationship
156 described by,

$$157 \log_{10} N = a - bM. \quad (1),$$

158 where N is the number of earthquakes greater than a magnitude M , and a and b are constants
159 describing the rate of seismicity and the relationship between the rate of smaller and larger
160 earthquakes, respectively. Globally, b -values are on average approximately 1.0 (El-Isa &
161 Eaton, 2014). Perturbations in b -value are thought to be linked to prevailing effective stress
162 conditions. Specifically, b -values greater than one are a result of processes that lower the
163 effective stress on a fault, such as an increase in pore pressure due to the presence of fluids
164 at the fault, for example (Schlaphorst et al., 2016). High b -values therefore indicate the
165 possible presence of fluid migration.

166

167 To calculate overall earthquake catalogue b -values, we use the method of Roberts et
168 al. (2015). Temporal variation in b -values are found using the method detailed in Roberts et

169 al. (2016), which has proved successful for other volcano seismology studies (Greenfield et
170 al., 2020). A full description of the methods used to calculate overall b-values and associated
171 temporal variations are provided in the Supplementary Material.

172

173 **2.5 Seismicity clustering analysis for delineating fault structure**

174 Clustering analysis is performed on the shallower seismicity above the APMB and
175 within 20 km of Uturuncu's summit. Our motivation for this is that this shallow seismicity
176 might delineate shallow fault structures that would be otherwise challenging to observe. An
177 approximation is made that if the seismicity in any given cluster is distributed along a single
178 fault, then the principle component vector of the earthquake hypocentres within the cluster
179 can be assumed to represent the orientation of a linear fault.

180

181 The first step of the seismicity clustering and fault analysis method is to cluster the
182 individual hypocentres into common clusters. There are many algorithms available to perform
183 this clustering. The Density-Based Spatial Clustering for Applications with Noise (DBSCAN)
184 algorithm of Ester et al. (1996) is applied to the data, as used in other seismicity clustering
185 studies (for example, Cesca, 2020). This algorithm is appropriate for our spatial clustering
186 problem since it is effective for 3D geometries with clusters of varying density and size. It also
187 performs well compared to other methods for many samples with a number of clusters. The
188 method groups together points that are densely distributed in space and separated by
189 sparsely populated regions. Specifically the method comprises of the following steps:

- 190 1. First the algorithm selects a core sample. A core sample is defined as a sample that
191 is surrounded by a minimum number of samples, n_{min} , within a maximum
192 neighbourhood distance, d_{max} .

193 2. The algorithm then checks if each of the neighbouring points fulfil the
194 aforementioned criteria to be a core sample. This process is repeated for all core
195 samples to grow the cluster.

196 3. Steps (1) and (2) are repeated for randomly sampled points until all the data points
197 are processed and either labelled in clusters, or as noise points that do not belong
198 to a cluster.

199 The density of the clusters, and the algorithm performance, are therefore constrained by the
200 parameters n_{min} and d_{max} . We set n_{min} to be 5. d_{max} is set to be 0.5 km, based on optimising
201 the maximum number of clusters with the minimum number of unclustered earthquakes (see
202 Supplementary Figure S4).

203

204 Once the earthquakes are clustered, Principal Component Analysis (PCA) is used to
205 find the vector that represents the orientation of the cluster. If one assumes that the cluster
206 represents seismicity along a fault, and that the fault is linear, then this vector represents the
207 orientation of the fault. A summary of the PCA method applied to each cluster is as follows:

- 208 1. The data is standardised by demeaning and dividing by the standard deviation.
- 209 2. The covariance of this standardised data is then calculated.
- 210 3. Finally, the eigenvalues and eigenvectors of the covariance matrix are calculated,
211 with the eigenvector corresponding to the largest eigenvalue defining the
212 principal component vector of the cluster, and therefore the fault orientation.

213

214

215

216

217 **3. Results**

218 Figure 1 shows the seismicity observed at Uturuncu from 2009 to 2012. The
219 hypocentral depths of the shallow seismicity, less than 5 km bsl in Figure 1b, are distributed
220 with a mean depth of ~ 0 km bsl, resolving the depth discrepancy between earthquake depths
221 in Jay, et al. (2012) and Kukarina et al. (2017), which is shown explicitly in Pritchard et al.
222 (2018). This shallow seismicity is generally located within 5 km laterally of the Uturuncu's
223 summit. However, there are a number of distinct clusters of seismicity laterally offset by up
224 to 20 km, approximately to the SE, S, W and NW. The majority of clusters of seismicity have
225 approximately linear spatial distributions, oriented vertically or sub-vertically. There is no
226 obvious temporal behaviour linking the individual clusters, aside from earthquakes thought
227 to be triggered by the magnitude 8 Maule earthquake, Chile (Jay, et al., 2012) (yellow events,
228 Figure 1), which occurred on 27th February 2010. However, although the activation of each
229 cluster is apparently temporally random, each distinct spatial cluster is active only for a short
230 period of time, of the order of 10s of days, before shutting off again.

231

232 We observe a gap in seismicity at depths between approximately 14 to 22 km bsl, see
233 Figure 1a, below which considerable activity at depths between 22 to 50 km bsl is observed.
234 This deeper seismicity appears to show a distinct spatial-temporal trend, with the majority of
235 deep seismicity directly under Uturuncu occurring in 2010, likely triggered by the Maule
236 earthquake. Much of the deeper seismicity to the NW occurs later. While there could be a
237 physical cause of this observation for the seismicity directly under Uturuncu, the spatial-
238 temporal trend of seismicity offset to the NW is likely a result of the ANDIVOLC network
239 aperture not being sufficiently large to provide adequate earthquake detection and

240 hypocentral constraint in this region compared to the PLUTONS network, which has a wider
241 aperture.

242

243 Figure 2 shows examples of the displacement spectra used to calculate the moment
244 magnitudes for two earthquakes, of magnitudes 2.8 and 1.5. These events exemplify the
245 spectra of the largest and smallest events detected. The observed spectra for each event are
246 similar for each of the four stations shown in Figure 2a-d. The blue and red solid lines show
247 the observed spectra for the large and small event, respectively, with the noise, shown by the
248 grey lines, removed. For the larger event, the signal dominates over the noise at lower
249 frequencies, with the noise having a negligible effect on the long-period spectral level and
250 hence the moment magnitude. The same statement is also generally valid for the smaller
251 event at most stations, although in this case, the signal at station PLRR, Figure 2c, is clearly
252 effected by the noise. The corner frequencies for the smaller event are likely underestimated
253 due to the loss of high frequency signals below the noise (Butcher et al., 2020). However, with
254 the noise removed, the Brune model fit, shown by the dashed lines in Figure 2, provides a
255 good fit for the long-period spectral level all the data. This provides us with confidence that
256 our observed long-period spectral levels, and hence moment magnitudes, are robust for the
257 range of magnitude observed here.

258

259 The moment magnitude earthquake cumulative frequency distribution for the entire
260 Uturuncu seismicity catalogue is shown by the black points in Figure 3. The green points show
261 the values of the individual bins for the moment magnitude data. The best fitting Gutenberg-
262 Richter relationship is indicated by the blue line. The best fitting parameters are found using
263 the BVS method (Roberts et al., 2015), with a magnitude of completeness of 2.28 and a b-

264 value of 1.44 for 2,363 earthquakes. Similar analysis for the individual ANDIVOLC and
265 PLUTONS networks, as well as the data excluding earthquakes triggered by the 2010 Maule,
266 Chile, earthquake, gives similar b-values, all greater than one (see Supplementary Figure S2).
267 Local magnitudes for the Uturnuncu seismicity catalogue give a b-value of 0.80 for a magnitude
268 of completeness of 0.99 using the BVS method with the same parameters. This b-value of
269 0.80 is in stark contrast with the value of 1.44 from the moment magnitude data.

270

271 Temporal variation in earthquake moment magnitudes and b-values of sub-regions of
272 the study area are also investigated. Temporal variation of moment release and b-values are
273 shown in Figure 4. The two regions are defined in Figure 4a. Figure 4b shows the number of
274 events per day and the cumulative moment release through time. The triggered events on
275 the 27th February 2010 from the Maule earthquake can be clearly seen, with significant
276 moment release occurring over a duration of only a few days. The shallow system, Region 1,
277 appears to have an otherwise relatively stable release of seismic energy through time.
278 However, the deeper seismicity in Region 2 releases seismic energy sporadically, releasing
279 significantly more seismic energy in mid 2011 than early 2011, before tailing off again later
280 that year. Figure 4c shows the magnitude of completeness of the catalogue through time
281 compared to the typical noise level during the observation period. M_{noise} is defined here as
282 the moment magnitude of a hypothetical earthquake with long-period spectral level equal to
283 the seismogram noise level at a distance of 30 km from a receiver. Obviously the assumed
284 distance affects the result, but not by more than one order of magnitude for our range of
285 possible hypocentral distances. Although there are several periods of higher noise levels, the
286 noise is typically significantly below the magnitude of completeness level throughout the
287 study period. Figure 4c and Figure 4d show the temporal variation in b-value for Regions 1

288 and 2, respectively. The gold line shows when the network transitioned from the ANDIVOLC
289 to the PLUTONS network. The lower b-values observed by the ANDIVOLC network before
290 2010 are thought to be network effects, affecting the overall magnitude of completeness and
291 so shouldn't be interpreted in any detail. Although the dataset does have a sufficient number
292 of events to perform temporal b-value analysis, it is likely at the lower limit, and so short
293 period temporal variations should be treated cautiously. However, we can confirm that both
294 Regions 1 and 2 have b-values greater than one for the majority of the study period, with
295 average b-values of 1.12 and 1.41, respectively. This is in contrast to previous studies (Jay, et
296 al., 2012; Maher & Kendall, 2018).

297

298 A final analysis is to interrogate any spatial clustering present in the shallow seismicity
299 observed in Region 1 of Figure 4. The motivation for this is to delineate any fault structures
300 and compare fault orientations to the prevailing stress regime and observed seismic
301 anisotropy at Uturuncu. The shallow seismicity clustering and fault orientation results are
302 shown in Figure 5. The DBSCAN method clusters the data into 28 clusters, as shown by the
303 different coloured scatter points in Figure 5a,b. While the majority of earthquakes are
304 clustered, there a small number of events that visually appear to be clusters but are not
305 clustered in our analysis. However, we prefer an automated clustering algorithm over
306 manual inclusion of all events because it is unbiased and is clear theoretical basis. There is
307 therefore greater confidence in the results for earthquakes that do cluster, while still
308 providing with an overall picture of possible faults delineated by this seismicity. It is also
309 worth noting that one cluster of events centred at ~ 2.5 km directly north of the Uturuncu
310 summit (see Figure 5a) is comprised of hundreds of events. Figure 5a,b also show the fault
311 PCA vectors in gold. These fault orientations indicate that the PCA method provides a useful

312 method of determining the orientation of the clusters in three-dimensions. Here, the
313 approximation is made that these PCA vectors represent linear-approximated fault
314 orientations. Figure 5c shows the fault strikes for these PCA vector orientations. The Rose
315 diagram shows the number of faults in 10° bins. There are predominantly two fault
316 directions: the first NE-SW; and the second approximately perpendicular, with a NW-SE
317 strike. This is in broad agreement with the anisotropy results of Maher & Kendall, (2018),
318 shown by the red bins in Figure 5c. Fault dips are also shown relative to vertical. The fault
319 dips are observed to be almost all far from vertical, with a dominant orientation of 50° to
320 60° from vertical.

321

322 **4. Discussion**

323 **1.1 The importance of magnitude scale for b-values**

324 Before the implications and interpretation of our results for Uturuncu are discussed
325 specifically, we emphasise the importance of, and justification for, using the moment
326 magnitude scale rather than local magnitudes. Our results clearly show the difference in b-
327 value measurements using local vs. moment magnitude scales. B-values > 1 are found when
328 using moment magnitudes, compared to values < 1 observed using local magnitudes. This
329 difference in b-value is significant, as it suggests a completely different crustal stress regime.
330 With a b-value > 1 suggesting lower than expected normal stresses on the faults, resulting in
331 more smaller magnitude earthquakes than for tectonic seismicity, in contrast to a b-value < 1
332 corresponding to higher than expected normal stresses. This discrepancy has significant
333 implications for the identification of the causative processes of such seismicity, as evidenced
334 later in this study. The question this disagreement raises is: which measure provides an
335 accurate, valid measure of b-value?

336

337 We suggest that moment magnitude is the correct measure to use for b-value
338 analyses, and that local magnitude derived b-values should be treated with caution. The most
339 compelling justification for this is the theoretical basis for a break in the scaling factor of M_L
340 and M_w for smaller earthquakes compared to larger earthquakes. A study by Deichmann
341 (2017) uses observations and models to show that the attenuation characteristics of the
342 medium cause the higher frequency energy of smaller earthquakes observed at a receiver to
343 be more highly attenuated relative to the energy observed from large earthquakes. This effect
344 manifests itself in the M_L scale since M_L uses the maximum amplitude of a seismic phase in
345 the time-domain, which can be effected by a loss of high frequency energy. In contrast, M_w
346 uses the long-period spectral level, which is approximately isolated from this effect until the
347 energy is extremely highly attenuated. This is likely the behaviour observed here, as is
348 observed in other data (Butcher et al., 2020), and is why M_w should be used over M_L if possible
349 in all instances, but especially in highly attenuating regions with low magnitude earthquakes,
350 such as at volcanoes.

351

352 Our results provide further evidence that M_w should be used, rather than M_L , for b-
353 value analyses. The moment magnitude is a physically meaningful measure, which does not
354 rely upon empirically derived correction terms that can vary by orders of magnitude.
355 Secondly, in our case the moment magnitudes are in close agreement with those calculated
356 from full waveform inversions of the same seismicity (Alvizuri & Tape, 2016) (see
357 Supplementary Figure S3). A further indication that moment magnitude might be a more
358 accurate, valid measure of b-value here is that it provides a b-value greater than one, which
359 is expected for volcanic systems with fluids present (Schlaphorst et al., 2016). Although b-

360 values less than one have been observed for the crust in the vicinity of volcanoes, regions of
361 fluid or partial melt at these volcanoes are found to have b-values greater than one (Farrell
362 et al., 2009; Greenfield et al., 2020; Murru et al., 2007; Power et al., 1998; Wiemer et al.,
363 1998; Wilks et al., 2017).

364

365 **4.2 New insights of Uturuncu**

366 Figure 6 summarises the seismic observations and the key interpretations of this
367 study, (1) to (6), which provide new insights into Uturuncu and the underlying crust. There
368 are six main conclusions from our findings, which help explain other geophysical and
369 geochemical observations (see Figure 7) and provide insights regarding the flow of fluids
370 through the crust. These findings are described below, with an explanation of how they fit
371 with other studies of Uturuncu.

372

373 (1) An absence of seismicity between ~14 to 22 km bsl (see Figure 1) delineates the
374 top and bottom of the ductile, elevated temperature signature of the APMB. The deeper
375 bound of this region was not observed clearly in previous studies (Jay, et al., 2012; Kukarina
376 et al., 2017) due to a lack of detected earthquakes and low confidence in the locations of
377 events that were detected. This absence of seismicity is likely a result of the crust within the
378 vicinity of the APMB being too hot and therefore too ductile to sustain the release of seismic
379 energy via brittle failure. The top of the APMB (see Figure 6), constrained by the absence of
380 seismicity, is in agreement with imaging of the APMB from ambient noise tomography,
381 receiver functions, and magnetotellurics (see Figure 7) (Chmielowski et al., 1999; Comeau et
382 al., 2016; Pritchard et al., 2018; Ward et al., 2014). Our observations also provide new

383 constraint on the bottom of the APMB, with seismicity observed at depths of greater than 22
384 km bsl, below the APMB.

385

386 The presence of a seismogenic zone beneath the APMB is an interesting result, since
387 it provides evidence for brittle, elastic crust rather than a melt-rich crust extending towards
388 the mantle. A natural question to then ask is what the origin of this seismicity is. The lack of
389 temporal migration of this seismicity, combined with the diffuse spatial, sub-horizontal
390 variation correlating with apparent fault structures suggests that this is not associated with
391 dike intrusion or vertical magma migration. Moment tensor inversions might provide
392 additional confirmation of this interpretation, although we do not pursue this here. An
393 alternative interpretation favoured here is that this seismicity is likely associated with
394 critically-stressed, fluid-rich faults. Evidence that the faults are critically-stressed is provided
395 by the significant additional seismicity triggered by stress perturbations due to the M8 Maule
396 earthquake. Evidence for fluid-rich faults is based upon high b-values, as discussed in
397 interpretation point (5), later in this text.

398

399 (2) The spatial distribution of seismicity suggests that the regional seismic brittle-
400 ductile transition zone is located at ~14 km bsl (purple dashed line, Figure 6), with a local
401 increase in the elevation of the brittle-ductile transition to ~4 km bsl (pink dashed line, Figure
402 6), approximately beneath Uturuncu's edifice. This local brittle-ductile transition zone depth
403 is consistent with the findings of Jay, et al. (2012). The depth of the brittle-ductile transition
404 zone is governed by crustal rheology, which itself is likely controlled by temperature. The ~14
405 km bsl depth of the regional brittle-ductile transition here is assumed to define the upper
406 possible extent of the elevated temperature APMB. Likewise, an increase in elevation of the

407 brittle-ductile transition to ~4 km bsl local to Uturuncu is likely caused by elevated
408 temperatures due to the presence of melt pockets, or perhaps hot saline fluids, connecting
409 the APMB to the shallower volcano. Approximate constraint for the depth of this brittle-
410 ductile transition zone is provided by clusters of seismicity, such as those laterally offset from
411 the summit of Uturuncu at longitudes of 67.23° N and 67.14 ° N. However, we cannot
412 confidently make further inferences on the topography of the brittle-ductile transition
413 without longer duration sampling of the seismicity. A shallow ductile region with elevated
414 crustal temperatures local to Uturuncu is consistent with a higher conductivity region
415 observed by magnetotelluric imaging (Comeau et al., 2016), a low density region (-150 kg m⁻³
416 density contrast) from gravity data extending from the APMB to approximately sea-level
417 (Del Potro et al., 2013), and the centre of a 70 km diameter area of uplift (Gottsmann et al.,
418 2018). Del Potro et al. (2013) suggest up to 25% partial melt within the low density body
419 ascending diapirically rather than via diking. There is no evidence for active diking at present,
420 as shown by the near-total absence of seismicity at that depth (Rubin, 1993). However, our
421 observation period is of insufficient duration to interrogate seismic vs. aseismic migration of
422 melt at this volcano. The observed uplift deformation has been investigated using geophysical
423 and petrological observations, combined with thermomechanical modelling (Gottsmann et
424 al., 2017). This modelling suggests that the uplift could be caused by either: an igneous mush
425 column extending from the APMB to 6 km bsl; or a hybrid column composed of an igneous
426 mush below a solidified and permeable body extending from the APMB to around sea-level.
427 Our observations cannot prove or disprove either hypothesis.

428

429 (3) Shallow seismicity delineates fault structures, indicated by the red solid lines in
430 Figure 6, derived from the seismicity clustering analysis presented in Figure 5. These clusters

431 of seismicity switch on and off randomly, with each cluster only active for an order of days to
432 tens of days at a time (see Figure 1). These clusters are approximately linear in geometry,
433 verifying that our linear-fault approximation is valid. The close agreement between the two
434 families of fault strikes and a previous study of anisotropy (Maher & Kendall, 2018) suggests
435 that observed anisotropy is primarily controlled by the faulting and/or orientations of the
436 stress regime. We cannot rule out faults with other orientations present at Uturuncu, but can
437 say that any such faults are not seismically active during the observation period, and so if they
438 do exist then they are likely locked by the crustal stress regime. Another interesting
439 observation is that the fault dips are not vertical or sub-vertical (see Figure 5d), as observed
440 at other volcanoes (Greenfield & White, 2015; Hudson et al., 2017; Lavayssière et al., 2019;
441 Shelly & Hill, 2011). This observation provides further evidence that the faulting is likely
442 controlled by the long wavelength stress regime driven by regional deformation, such as the
443 150 km diameter deformation anomaly observed by InSAR, GNSS and levelling (Gottsmann et
444 al., 2018). Furthermore, there is no observed systematic variation in the vertical orientation
445 of these faults focussed directly towards Uturuncu's summit that would be associated with
446 ring-faulting centred about a shallow deformation signal. Overall, the earthquake clustering
447 and PCA vector analysis shows that the seismicity clearly delineates fault structures, oriented
448 so as to accommodate perturbations in the crustal stress regime.

449

450 (4) High b-values (> 1) of the shallow seismicity in Region 1, local to Uturuncu, are
451 most likely associated with a reduction in the effective normal stress of the faults imaged in
452 (3). Such high b-values are observed at other volcanoes (Bridges & Gao, 2006; Greenfield et
453 al., 2018; Roberts et al., 2015). One possible cause of high b-values could be inflation reducing
454 the normal stress on the faults (Bridges & Gao, 2006). However, the general lack of any

455 spatial-temporal correlation in activity and apparent lack of interaction between the clusters
456 of seismicity discussed in (3) implies that the seismicity is not modulated primarily by the
457 crustal stress state, but by something in the immediate vicinity of the individual faults. It is
458 suggested that the reduced normal stresses on the faults are caused by elevated pore
459 pressures due to the trapping and/or migration of fluids within the fault systems (Schlaphorst
460 et al., 2016). This interpretation is consistent with the interpretations from seismic anisotropy
461 studies, suggesting fluids within the faults (Leidig & Zandt, 2003; Zandt et al., 2003), and
462 moment tensor analysis that suggests that the shallow (< 4 km bsl) seismicity within the
463 immediate vicinity of the volcano exhibits predominantly opening tensile cracks and opening
464 cracks with an explosive component (Alvizuri & Tape, 2016). Furthermore, this interpretation
465 might also explain the high electrical conductivity anomaly at shallow depths from
466 magnetotelluric measurements (Comeau et al., 2016).

467

468 Assuming that fluids do play a role in the shallow seismicity observed at Uturuncu, it
469 encourages the question: are the fluids melt, or water and/or other volatiles. It is suggested
470 that the shallow seismicity is associated with a hydrothermal system rather than melt for the
471 following reason. It is difficult to conceive of significant partial melt volumes this shallow in
472 the crust, without there being a surface expression of such melt. There is no evidence for
473 eruptive activity at Uturuncu in the last 250,000 years (Pritchard et al., 2018). It is therefore
474 assumed that the shallow system is hydrothermal, with some of the water to drive the
475 hydrothermal system possibly exsolved from either wet partial melt ascending from the
476 APMB or from the wet APMB itself (Laumonier et al., 2017), an migrating through the region
477 of elevated temperature depicted in Figure 6. This assumption of a hydrothermal system is

478 supported by observations of sulphur deposits, degassing, and surface thermal features, as
479 described in Pritchard et al. (2018).

480

481 (5) Earthquake b-values > 1 for Region 2 (as defined in Figure 4) suggest that much of
482 this seismicity is also associated with fluids. Given the spatial distribution of this seismicity, it
483 is suggested that this is again fluids, perhaps from the subducting slab at depths of 100 to 150
484 km bsl (Cahill & Isacks, 1992; Prezzi et al., 2009), trapped and/or migrating along pre-existing
485 faults, towards the APMB. This hypothesis is affirmed by the S-wave tomography results
486 (Kukarina et al., 2017) shown in Figure 7d, which show an anomalously low shear-velocity
487 region extending from the slab towards the deep seismicity we observe. This low velocity
488 zone continues upwards along the path of the seismicity towards the depth of the APMB. This
489 is an exciting result, since this seismicity is likely evidence of the migration of water from the
490 dehydrating subducting slab through the crust. If correct, this observation has implications
491 for where and how melt in the APMB originates, as well as the melt chemistry.

492

493 (6) Finally, for fluids to reach the shallow volcanic system, and likely the surface, they
494 would have to pass through the APMB and elevated temperature region, as shown by the
495 blue arrow in Figure 6. These fluids would travel aseismically here, due to insufficient strain
496 rates to cause elastic failure within the hot, ductile crust. Such fluid migration, whereby water-
497 rich andesitic melt and/or magmatic water travels from the APMB to the shallower partial
498 melt column structure beneath Uturuncu, is suggested in Gottsmann et al. (2017).

499

500 **4.3 Wider implications**

501 Our observation of seismicity associated with fluid migration throughout the crust
502 (conclusions (4) to (6)) has wider geological and economic implications. We assume here that
503 a substantial component of the fluid flux is slab-derived H₂O (Laumonier et al., 2017). This
504 ascent of water via percolation along faults would provide an additional route of fluid ascent
505 to that of magma ascent, such as that postulated in Collins et al. (2020). This additional water
506 ascent mechanism could have two critical implications. Firstly, it could enhance the water
507 content of magma in the APMB and Uturuncu volcanic system. Indeed, Laumonier et al.
508 (2017) show that the APMB has an unusually high water content ($\geq 8 \text{ wt. } \% \text{ H}_2\text{O}$). This water
509 content is important since H₂O degassing drives crystallisation, which increases the melt
510 viscosity, inhibiting the ascent of melt towards the surface. Therefore, if the fluid ascent
511 pathway that we observe can transport sufficient water to shallower melt storage regions,
512 then this mechanism could play a critical role for controlling arc volcanism and volcanic
513 eruptions. The second implication of the fluid ascent pathways is that it could facilitate the
514 transport of minerals from the slab to the shallow hydrothermal system (Manning, 2004). This
515 mechanism could promote enhanced mineral deposition at sufficiently shallow depths for
516 mining.

517

518 **Conclusions**

519 We present new analysis of seismicity at Uturuncu volcano from two seismic
520 experiments in operation between 2009 and 2012. The seismicity delineates: shallow fault
521 structures (< 4 km bsl) directly beneath Uturuncu; deeper seismicity below the APMB (>22
522 km bsl), defining a lower depth limit of the APMB, with this seismicity primarily laterally offset
523 to the NE of Uturuncu; a lack of seismicity constraining the location of the APMB; and a
524 shallower region above the APMB and below Uturuncu that is absent of seismicity. The APMB

525 therefore does not extend below ~24 km bsl, suggesting an underlying cooler, brittle crust.
526 This new analysis also reconciles a discordance in the distribution of earthquake depths for
527 the shallow seismicity directly beneath Uturuncu presented in previous studies. The shallow
528 region absent of seismicity directly below Uturuncu is interpreted to be a region of elevated
529 temperature, indicative of the presence of partial melt and/or the advective heat transport
530 by migrating fluids. Moment magnitudes are calculated for all the recorded seismicity. These
531 moment magnitudes provide estimates of b-values that are greater than one, as expected for
532 a hydrothermally active volcanic system. This is contrary to previous studies that used local
533 magnitudes to calculate b-values, with these studies finding b-values less than one. This result
534 emphasises the importance of using absolute moment magnitude rather than an empirical
535 local magnitude scale. Intriguingly, b-values are found to be greater than one in both the
536 shallow region directly beneath Uturuncu, and the deeper seismicity below the APMB. The
537 high b-values in the shallow region are interpreted to be caused by trapping and migration of
538 fluids along pre-existing faults, likely comprising a hydrothermal system. High b-values for the
539 deeper seismicity (25 to 50 km bsl) suggest ascent of fluids, whether that be melt and/or
540 water, from greater depths along a fault zone NE of Uturuncu. This seismicity likely elucidates
541 a pathway of fluids from the subducting slab towards the surface. These fluids likely migrate
542 upwards along fault zones from the slab, before travelling aseismically through the APMB and
543 shallower elevated temperature region. They then feed shallow hydrothermal systems,
544 where the fluids reduce the effective pressure on shallow faults, triggering the observed
545 shallow (< 4 km bsl) seismicity. These pathways of fluid ascent may provide a critical control
546 on the water-content of melt in the crust, and hence the risk of volcanic eruptions, as well as
547 promoting the accumulation of shallow mineral deposits.

548

549

550 **Acknowledgements**

551 We thank all the PLUTONS team for discussions relating to the interpretations that no doubt
552 improved this manuscript. We especially thank Ying Liu for providing her seismic velocity
553 model that was used to locate the seismicity in this study, as well as Patricia McQueen for
554 providing additional datasets from previous studies for producing the literature comparison
555 plots included in this study. The seismic data analysed in this study is publicly available from
556 IRIS. The earthquake detection algorithm used in this study, QuakeMigrate (Winder et al.,
557 2021), is available open source. We have also made the software used to calculate moment
558 magnitudes and b-values, SeisSrcMoment (Hudson, 2020), available open source. Some of
559 the figures were produced using Generic Mapping Tools (GMT) (Wessel et al., 2019). Much of
560 the seismic data analysis was performed using ObsPy (Beyreuther et al., 2010). This work, and
561 TSH were funded by the NSFGE0-NERC grant NE/S008845/1. JDB thanks the Royal Society for
562 financial support through a Research Professorship (RP\R1\201048). The seismic data
563 collection funded by the National Science Foundation grants 0908281 and 0909254, and the
564 UK Natural Environment Research Council grant NE/G01843X/1.

565

566

567

568

569

570

571

572

573

574 **References**

575 Alvizuri, C., & Tape, C. (2016). Full moment tensors for small events ($M_w < 3$) at Uturuncu
576 volcano, Bolivia. *Geophysical Journal International Advance Access Published July, 6*,
577 1761–1783. <https://doi.org/10.1093/gji/ggw247>

578 Beyreuther, M., Barsch, R., Krischer, L., Megies, T., Behr, Y., & Wassermann, J. (2010).
579 ObsPy: A Python Toolbox for Seismology. *Seismological Research Letters*, 81(3), 530–
580 533. <https://doi.org/10.1785/gssrl.81.3.530>

581 Bridges, D., & Gao, S. (2006). Spatial variation of seismic b-values beneath Makushin
582 Volcano, Unalaska Island, Alaska. *Earth and Planetary Science Letters*, 245(1–2), 408–
583 415. <https://doi.org/10.1016/j.epsl.2006.03.010>

584 Butcher, A., Lockett, R., Kendall, J.-M., & Baptie, B. (2020). Seismic Magnitudes, Corner
585 Frequencies, and Microseismicity: Using Ambient Noise to Correct for High-Frequency
586 Attenuation. *Bulletin of the Seismological Society of America*, 110(3), 1260–1275.
587 <https://doi.org/10.1785/0120190032>

588 Cahill, T., & Isacks, B. L. (1992). Seismicity and shape of the subducted Nazca Plate. *Journal*
589 *of Geophysical Research*, 97(B12). <https://doi.org/10.1029/92jb00493>

590 Cesca, S. (2020). Seiscloud, a tool for density-based seismicity clustering and visualization.
591 *Journal of Seismology*, 24(3), 443–457. <https://doi.org/10.1007/s10950-020-09921-8>

592 Chmielowski, J., Zandt, G., & Haberland, C. (1999). The central Andean Altiplano-Puna
593 magma body. *Geophysical Research Letters*, 26(6), 783–786.
594 <https://doi.org/10.1029/1999GL900078>

595 Collins, W. J., Murphy, J. B., Johnson, T. E., & Huang, H. Q. (2020). Critical role of water in the
596 formation of continental crust. *Nature Geoscience*, 13(5), 331–338.

- 597 <https://doi.org/10.1038/s41561-020-0573-6>
- 598 Comeau, M. J., Unsworth, M. J., & Cordell, D. (2016). New constraints on the magma
599 distribution and composition beneath Volcán Uturuncu and the southern Bolivian
600 Altiplano from magnetotelluric data. *Geosphere*, 12(5), 1391–1421.
601 <https://doi.org/10.1130/GES01277.1>
- 602 Deichmann, N. (2017). Theoretical basis for the observed break in ML/MW scaling between
603 small and large earthquakes. *Bulletin of the Seismological Society of America*, 107(2),
604 505–520. <https://doi.org/10.1785/0120160318>
- 605 Drew, J., White, R. S., Tilmann, F., & Tarasewicz, J. (2013). Coalescence microseismic
606 mapping. *Geophysical Journal International*, 195(3), 1773–1785.
607 <https://doi.org/10.1093/gji/ggt331>
- 608 El-Isa, Z. H., & Eaton, D. W. (2014). Spatiotemporal variations in the b-value of earthquake
609 magnitude-frequency distributions: Classification and causes. *Tectonophysics*, 615–616,
610 1–11. <https://doi.org/10.1016/j.tecto.2013.12.001>
- 611 Ester, M., Kriegel, H.-P., Sander, J., & Xu, X. (1996). A Density-Based Algorithm for
612 Discovering Clusters in Large Spatial Databases with Noise. In *KDD-96 Proceedings* (pp.
613 226–231). Elsevier. Retrieved from
614 <https://linkinghub.elsevier.com/retrieve/pii/B9780444527011000673>
- 615 Farrell, J., Husen, S., & Smith, R. B. (2009). Earthquake swarm and b-value characterization
616 of the Yellowstone volcano-tectonic system. *Journal of Volcanology and Geothermal
617 Research*, 188(1–3), 260–276. <https://doi.org/10.1016/j.jvolgeores.2009.08.008>
- 618 Gottsmann, J., Blundy, J., Henderson, S., Pritchard, M. E., & Sparks, R. S. J. (2017).
619 Thermomechanical modeling of the altiplano-puna deformation anomaly:
620 Multiparameter insights into magma mush reorganization. *Geosphere*, 13(4), 1042–

- 621 1045. <https://doi.org/10.1130/GES01420.1>
- 622 Gottsmann, Joachim, del Potro, R., & Muller, C. (2018). 50 years of steady ground
623 deformation in the Altiplano-Puna region of southern Bolivia. *Geosphere*, *14*(1), 65–73.
624 <https://doi.org/10.1130/GES01570.1>
- 625 Greenfield, T., & White, R. S. (2015). Building Icelandic igneous crust by repeated melt
626 injections. *Journal of Geophysical Research: Solid Earth*, *120*(11), 7771–7788.
627 <https://doi.org/10.1002/2015JB012009>
- 628 Greenfield, T., White, R. S., Winder, T., & Ágústsdóttir, T. (2018). Seismicity of the Askja and
629 Bárðarbunga volcanic systems of Iceland, 2009–2015. *Journal of Volcanology and*
630 *Geothermal Research*, (xxxx), 2009–2015.
631 <https://doi.org/10.1016/j.jvolgeores.2018.08.010>
- 632 Greenfield, T., White, R. S., Winder, T., & Ágústsdóttir, T. (2020). Seismicity of the Askja and
633 Bardarbunga volcanic systems of Iceland, 2009–2015. *Journal of Volcanology and*
634 *Geothermal Research*, *391*. <https://doi.org/10.1016/j.jvolgeores.2018.08.010>
- 635 Hanks, T. C., & Kanamori, H. (1979). A moment magnitude scale. *Journal of Geophysical*
636 *Research*, *84*(B5), 2348. <https://doi.org/10.1029/JB084iB05p02348>
- 637 Henderson, S. T., & Pritchard, M. E. (2017). Time-dependent deformation of Uturuncu
638 volcano, Bolivia, constrained by GPS and InSAR measurements and implications for
639 source models. *Geosphere*, *13*(6), 1834–1854. <https://doi.org/10.1130/GES01203.1>
- 640 Hudson, T. S., White, R. S., Greenfield, T., Ágústsdóttir, T., Brisbane, A., & Green, R. G.
641 (2017). Deep crustal melt plumbing of Bárðarbunga volcano, Iceland. *Geophysical*
642 *Research Letters*, *44*(17), 8785–8794. <https://doi.org/10.1002/2017GL074749>
- 643 Hudson, T.S. (2020). TomSHudson/SeisSrcMoment: First formal release (Version 1.0.0).
644 *Zenodo*. <https://doi.org/http://doi.org/10.5281/zenodo.4010325>

- 645 Hudson, Thomas S, Smith, J., Brisbourne, A., & White, R. (2019). Automated detection of
646 basal icequakes and discrimination from surface crevassing. *Annals of Glaciology*,
647 60(79), 1–11.
- 648 Hutchinson, L. (2015). *Double-Difference Relocation of Earthquakes at Uturuncu Volcano,*
649 *Bolivia, and Interior Alaska. MS Thesis, University of Alaska Fairbanks.*
- 650 Jay, J. A., Pritchard, M. E., West, M. E., Christensen, D., Haney, M., Minaya, E., et al. (2012).
651 Shallow seismicity, triggered seismicity, and ambient noise tomography at the long-
652 dormant Uturuncu Volcano, Bolivia. *Bulletin of Volcanology*, 74(4), 817–837.
653 <https://doi.org/10.1007/s00445-011-0568-7>
- 654 Kukarina, E., West, M., Keyson, L. H., Koulakov, I., Tsibizov, L., & Smirnov, S. (2017). Focused
655 magmatism beneath Uturuncu volcano, Bolivia: Insights from seismic tomography and
656 deformation modeling. *Geosphere*, 13(6), 1855–1866.
657 <https://doi.org/10.1130/GES01403.1>
- 658 Laumonier, M., Gaillard, F., Muir, D., Blundy, J., & Unsworth, M. (2017). Giant magmatic
659 water reservoirs at mid-crustal depth inferred from electrical conductivity and the
660 growth of the continental crust. *Earth and Planetary Science Letters*, 457, 173–180.
661 <https://doi.org/10.1016/j.epsl.2016.10.023>
- 662 Lavayssière, A., Greenfield, T., Keir, D., Ayele, A., & Kendall, J. M. (2019). Local seismicity
663 near the actively deforming Corbetti volcano in the Main Ethiopian Rift. *Journal of*
664 *Volcanology and Geothermal Research*, 381(January 2016), 227–237.
665 <https://doi.org/10.1016/j.jvolgeores.2019.06.008>
- 666 Leidig, M., & Zandt, G. (2003). Modeling of highly anisotropic crust and application to the
667 Altiplano-Puna volcanic complex of the central Andes. *Journal of Geophysical Research:*
668 *Solid Earth*, 108(B1), ESE 5-1-ESE 5-15. <https://doi.org/10.1029/2001jb000649>

- 669 Lomax, A., & Virieux, J. (2000). Probabilistic earthquake location in 3D and layered models.
670 *Advances in Seismic Event Location, Volume 18 of the Series Modern Approaches in*
671 *Geophysics*, 101–134.
- 672 Maher, S., & Kendall, J. (2018). Crustal anisotropy and state of stress at Uturuncu Volcano ,
673 Bolivia , from shear-wave splitting measurements and magnitude – frequency
674 distributions in seismicity. *Earth and Planetary Science Letters*, 495, 38–49.
675 <https://doi.org/10.1016/j.epsl.2018.04.060>
- 676 Manning, C. E. (2004). The chemistry of subduction-zone fluids. *Earth and Planetary Science*
677 *Letters*, 223(1–2), 1–16. <https://doi.org/10.1016/j.epsl.2004.04.030>
- 678 Muir, D. D., Barfod, D. N., Blundy, J. D., Rust, A. C., Sparks, R. S. J., & Clarke, K. M. (2015). The
679 temporal record of magmatism at Cerro Uturuncu, Bolivian Altiplano. *Geological*
680 *Society Special Publication*, 422(1), 57–83. <https://doi.org/10.1144/SP422.1>
- 681 Murru, M., Console, R., Falcone, G., Montuori, C., & Sgroi, T. (2007). Spatial mapping of the
682 b value at Mount Etna, Italy, using earthquake data recorded from 1999 to 2005.
683 *Journal of Geophysical Research: Solid Earth*, 112(12), 1–15.
684 <https://doi.org/10.1029/2006JB004791>
- 685 Del Potro, R., Díez, M., Blundy, J., Camacho, A. G., & Gottsmann, J. (2013). Diapiric ascent of
686 silicic magma beneath the Bolivian Altiplano. *Geophysical Research Letters*, 40(10),
687 2044–2048. <https://doi.org/10.1002/grl.50493>
- 688 Power, J. A., Wyss, M., & Latchman, J. L. (1998). Spatial variations in the frequency-
689 magnitude distribution. *Geophysical Research Letters*, 25(19), 3653–3656.
- 690 Prezzi, C. B., Götze, H. J., & Schmidt, S. (2009). 3D density model of the Central Andes.
691 *Physics of the Earth and Planetary Interiors*, 177(3–4), 217–234.
692 <https://doi.org/10.1016/j.pepi.2009.09.004>

- 693 Pritchard, M. E., de Silva, S. L., Michelfelder, G., Zandt, G., McNutt, S. R., Gottsmann, J., et al.
694 (2018). Synthesis: PLUTONS: Investigating the relationship between pluton growth and
695 volcanism in the Central Andes. *Geosphere*, 14(3), 954–982.
696 <https://doi.org/10.1130/GES01578.1>
- 697 Roberts, N. S., Bell, A. F., & Main, I. G. (2015). Are volcanic seismic b-values high, and if so
698 when? *Journal of Volcanology and Geothermal Research*, 308, 127–141.
699 <https://doi.org/10.1016/j.jvolgeores.2015.10.021>
- 700 Roberts, N. S., Bell, A. F., & Main, I. G. (2016). Mode switching in volcanic seismicity: El
701 Hierro 2011–2013. *Geophysical Research Letters*, 43(9), 4288–4296.
702 <https://doi.org/10.1002/2016GL068809>
- 703 Rubin, A. M. (1993). Dikes vs. diapirs in viscoelastic rock. *Earth and Planetary Science*
704 *Letters*, 117(3–4), 653–670. [https://doi.org/10.1016/0012-821X\(93\)90109-M](https://doi.org/10.1016/0012-821X(93)90109-M)
- 705 Schlaphorst, D., Kendall, J. M., Collier, J. S., Verdon, J. P., Blundy, J., Baptie, B., et al. (2016).
706 Water, oceanic fracture zones and the lubrication of subducting plate boundaries-
707 insights from seismicity. *Geophysical Journal International*, 204(3), 1405–1420.
708 <https://doi.org/10.1093/gji/ggv509>
- 709 Schmitz, M., Heinsohn, W. D., & Schilling, F. R. (1997). Seismic, gravity and petrological
710 evidence for partial melt beneath the thickened Central Andean crust (21–23°S).
711 *Tectonophysics*, 270(3–4), 313–326. [https://doi.org/10.1016/S0040-1951\(96\)00217-X](https://doi.org/10.1016/S0040-1951(96)00217-X)
- 712 Shelly, D. R., & Hill, D. P. (2011). Migrating swarms of brittle-failure earthquakes in the lower
713 crust beneath Mammoth Mountain, California. *Geophysical Research Letters*, 38(20),
714 1–6. <https://doi.org/10.1029/2011GL049336>
- 715 Smith, J. D., White, R. S., Avouac, J.-P., & Bourne, S. (2020). Probabilistic earthquake
716 locations of induced seismicity in the Groningen region, the Netherlands. *Geophysical*

- 717 *Journal International*, 222(1), 507–516. <https://doi.org/10.1093/gji/ggaa179>
- 718 Sparks, R. S. J., Folkes, C. B., Humphreys, M. C. S., Barfod, D. N., Clavero, J., Sunagua, M. C.,
719 et al. (2008). Uturuncu volcano, Bolivia: Volcanic unrest due to mid-crustal magma
720 intrusion. *American Journal of Science*, 308(6), 727–769.
721 <https://doi.org/10.2475/06.2008.01>
- 722 Ward, K. M., Porter, R. C., Zandt, G., Beck, S. L., Wagner, L. S., Minaya, E., & Tavera, H.
723 (2013). Ambient noise tomography across the Central Andes. *Geophysical Journal*
724 *International*, 194(3), 1559–1573. <https://doi.org/10.1093/gji/ggt166>
- 725 Ward, K. M., Zandt, G., Beck, S. L., Christensen, D. H., & McFarlin, H. (2014). Seismic imaging
726 of the magmatic underpinnings beneath the Altiplano-Puna volcanic complex from the
727 joint inversion of surface wave dispersion and receiver functions. *Earth and Planetary*
728 *Science Letters*, 404, 43–53. <https://doi.org/10.1016/j.epsl.2014.07.022>
- 729 Wessel, P., Luis, J. F., Uieda, L., Scharroo, R., Wobbe, F., Smith, W. H. F., & Tian, D. (2019).
730 The Generic Mapping Tools Version 6. *Geochemistry, Geophysics, Geosystems*, 20(11),
731 5556–5564. <https://doi.org/10.1029/2019GC008515>
- 732 Wiemer, S., McNutt, S. R., & Wyss, M. (1998). Temporal and three-dimensional spatial
733 analyses of the frequency-magnitude distribution near Long Valley Caldera, California.
734 *Geophysical Journal International*, 134(2), 409–421. [https://doi.org/10.1046/j.1365-](https://doi.org/10.1046/j.1365-246X.1998.00561.x)
735 [246X.1998.00561.x](https://doi.org/10.1046/j.1365-246X.1998.00561.x)
- 736 Wilks, M., Kendall, J. M., Nowacki, A., Biggs, J., Wookey, J., Birhanu, Y., et al. (2017).
737 Seismicity associated with magmatism, faulting and hydrothermal circulation at Aluto
738 Volcano, Main Ethiopian Rift. *Journal of Volcanology and Geothermal Research*, 340,
739 52–67. <https://doi.org/10.1016/j.jvolgeores.2017.04.003>
- 740 Winder, T., Bacon, C., Smith, J. D., Hudson, T. S., Drew, J., & White, R. S. (2021).

741 QuakeMigrate v1.0.0. *Zenodo*. <https://doi.org/10.5281/zenodo.4442749>

742 Zandt, G., Leidig, M., Chmielowski, J., Baumont, D., & Yuan, X. (2003). Seismic detection and

743 characterization of the Altiplano-Puna magma body, Central Andes. *Pure and Applied*

744 *Geophysics*, 160(3–4), 789–807. <https://doi.org/10.1007/PL00012557>

745

746

747

748

749

750

751

752

753

754

755

756

757

758

759

760

761

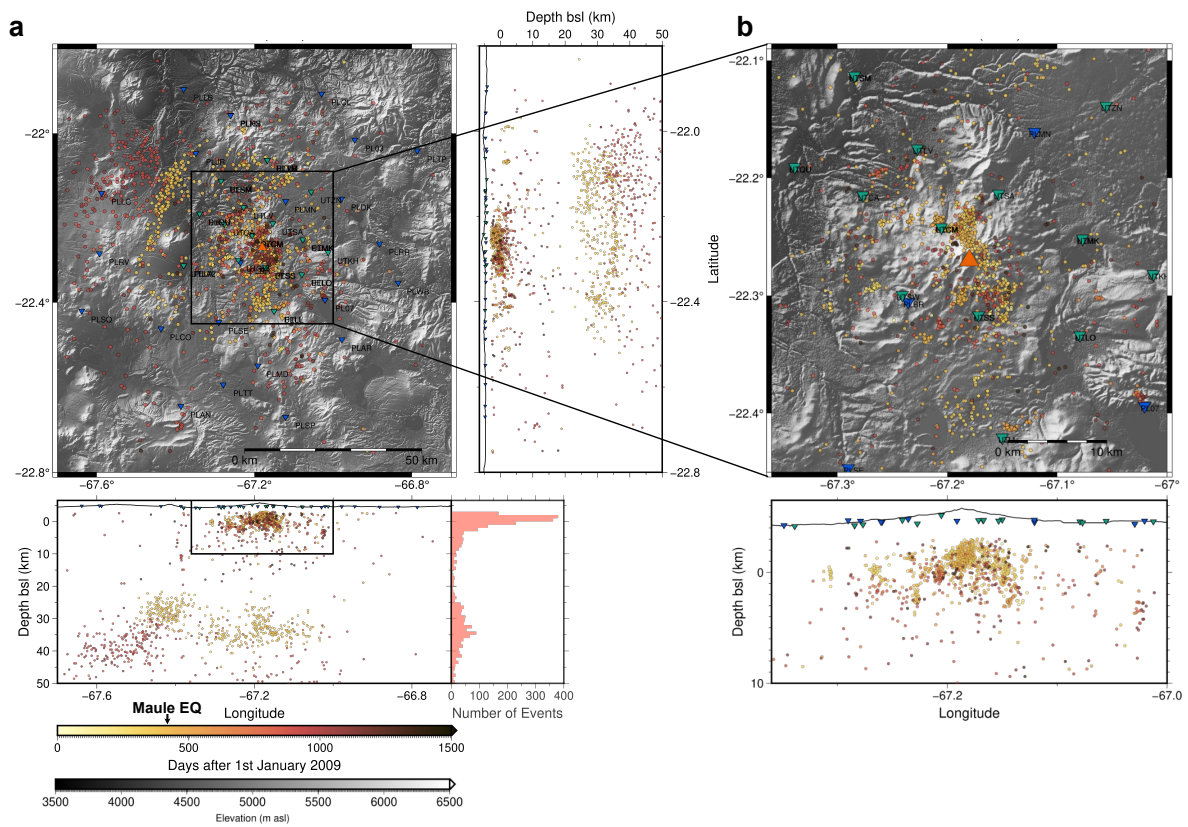
762

763

764

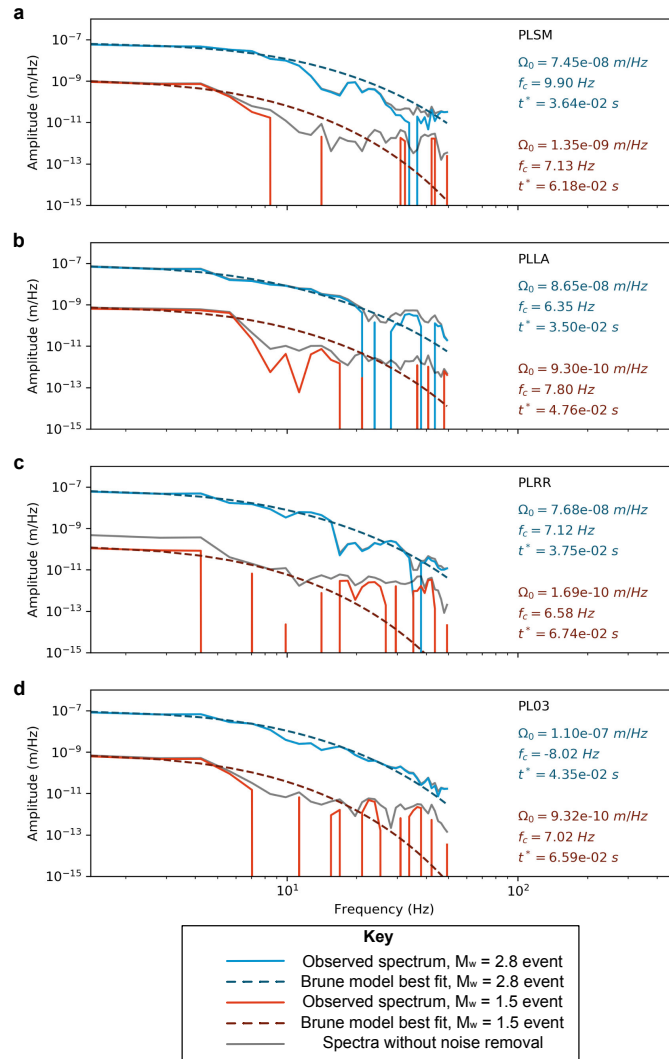
765 **Figures**

766



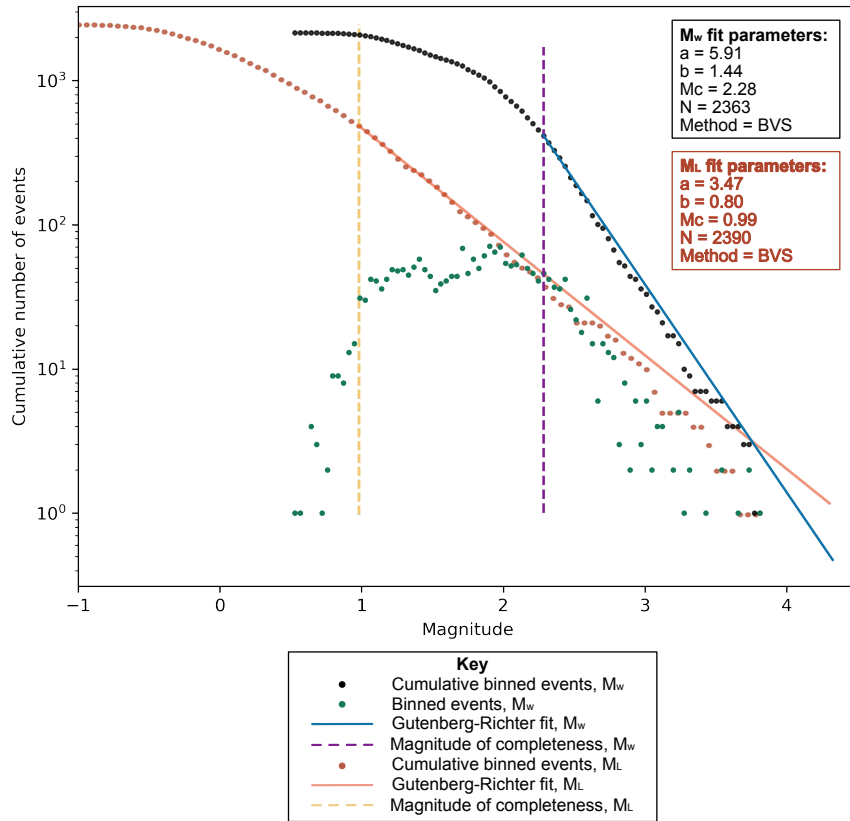
767

768 *Figure 1 – Seismicity observed at Uturuncu between 2009 and 2012. a) Map of overall seismicity observed in the region*
 769 *surrounding Uturuncu, as well as latitude and longitude depth profiles. The summit of Uturuncu is shown by the orange*
 770 *triangle. Seismometers are shown by the green (ANDIVOLC) and blue (PLUTONS) inverted triangles. Depth profiles are taken*
 771 *through the summit of the volcano. Events are coloured by time. Note the significant rate of triggered seismicity due to the*
 772 *Maule earthquake, labelled on the time colour legend. b) Enlarged map and longitude depth profile of the seismicity in the*
 773 *immediate vicinity of Uturuncu.*



774

775 Figure 2 – Examples of earthquake source displacement spectra for two events at four stations: PLSM, PLLA, PLRR and PL03,
 776 labelled (a) to (d), respectively. Both events are located in the immediate vicinity of Uturunco, as defined by Figure 1b. The
 777 first event is a $M_w = 2.8$ event, shown in blue, and the second event is a $M_w = 1.5$ event, shown in red. The solid lines show the
 778 observed spectra and the dashed lines show the best fitting Brune model. The grey lines show the spectra prior to noise
 779 removal.



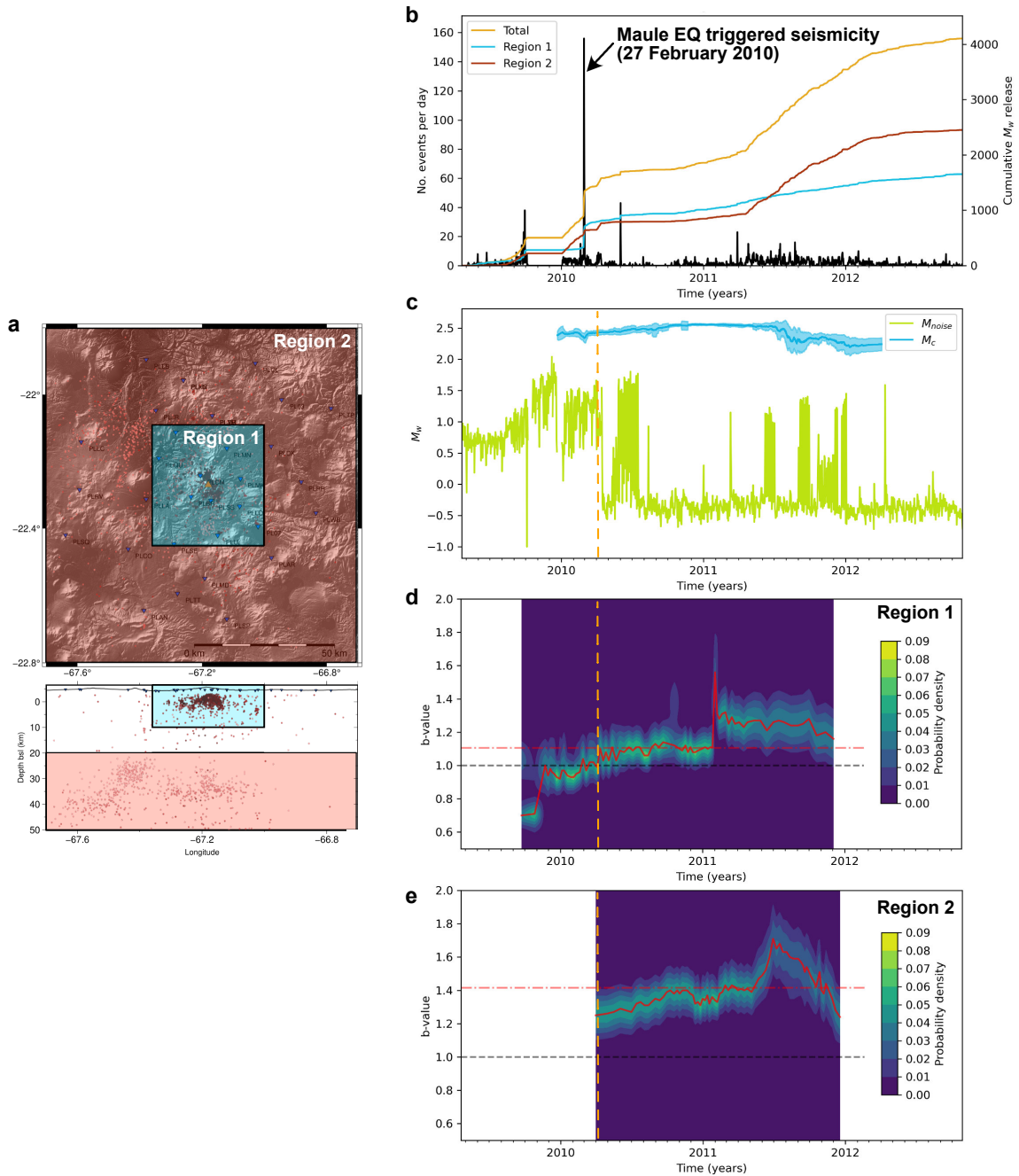
780

781 *Figure 3 – Gutenberg-Richter plot of cumulative number of events vs. magnitude. The moment magnitude, M_w , catalogue is*
 782 *plotted in black. The local magnitude catalogue is plotted for comparison in red. Magnitudes of completeness for the*
 783 *respective catalogues are shown by the dashed lines.*

784

785

786



787

788 *Figure 4 – Temporal variation in earthquake magnitudes and b-values. a) Map and depth profile defining the two regions*

789 *used in (b), (d) and (e). b) Plot of number of events per day and cumulative moment magnitude release per day through time.*

790 *c) Plot of magnitude of completeness through time compared to the representative daily noise level. The noise level is*

791 *measured at 12:01 UTC each day, for an assumed epicentral distance of 30 km and an isotropic radiation pattern. d) Plot of*

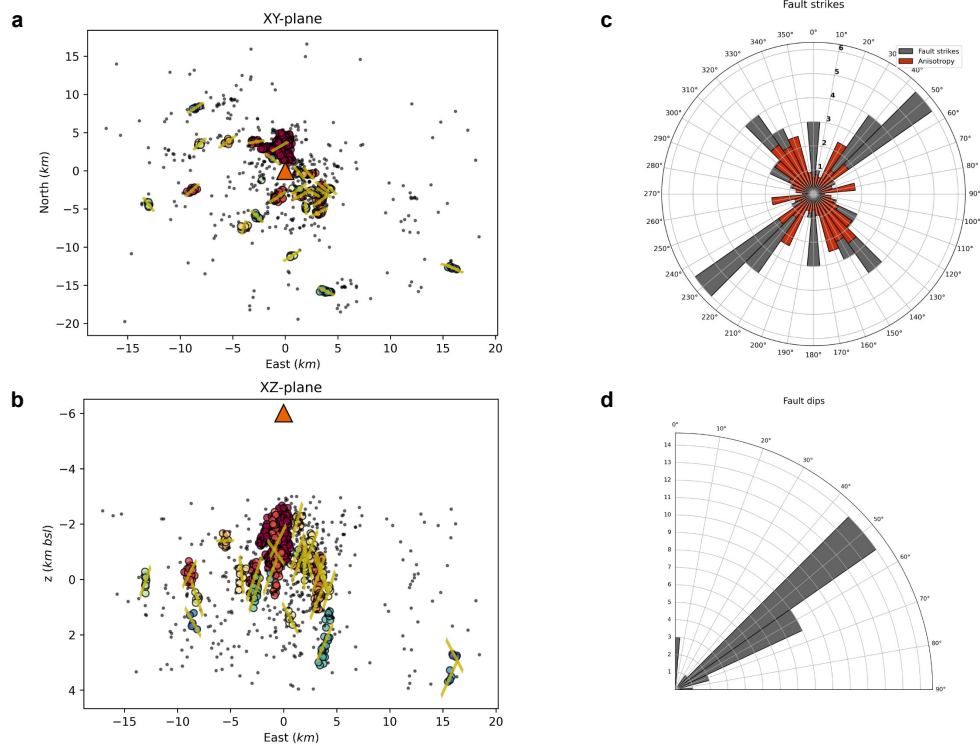
792 *b-value through time for region 1, using the method described in Roberts et al (2016). e) Same as (d), but for region 2. 5000*

793 *random windows of sizes 50 to 500 are used to obtain the temporal b-value variation. We stack every 10 samples to smooth*

794 *the PDFs. The black line indicates $b = 1$. The orange line indicates when the seismic network transitioned from the ANDIVOLC*

795 *network to the PLUTONS network.*

796



797

798 *Figure 5 - Shallow seismicity fault cluster analysis. a) Map of horizontal spatial distribution of seismicity, coloured by cluster*
 799 *(28 clusters in total). Principal axes of the clusters plotted by gold lines from PCA analysis. Orange triangle shows the location*
 800 *of the summit of Uturuncu. b) Same as (a) but for an East-West depth profile. c) Rose diagram showing the orientation of the*
 801 *principal component vectors' strikes in black. Red data show the anisotropy results of Maher and Kendall (2018) for*
 802 *comparison. d) Rose diagram showing the dips of the faults from vertical (up is positive). Note that the anisotropy data plotted*
 803 *in (c) is scaled simply to provide a comparison of orientation rather than magnitude of anisotropy.*

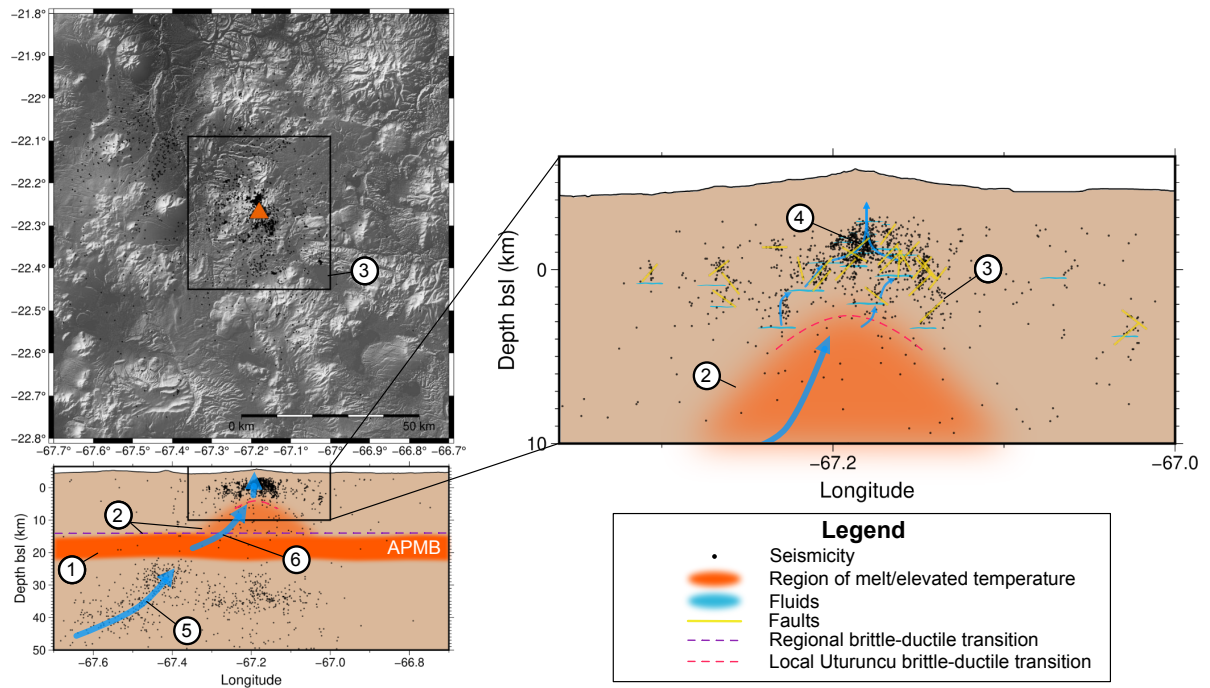
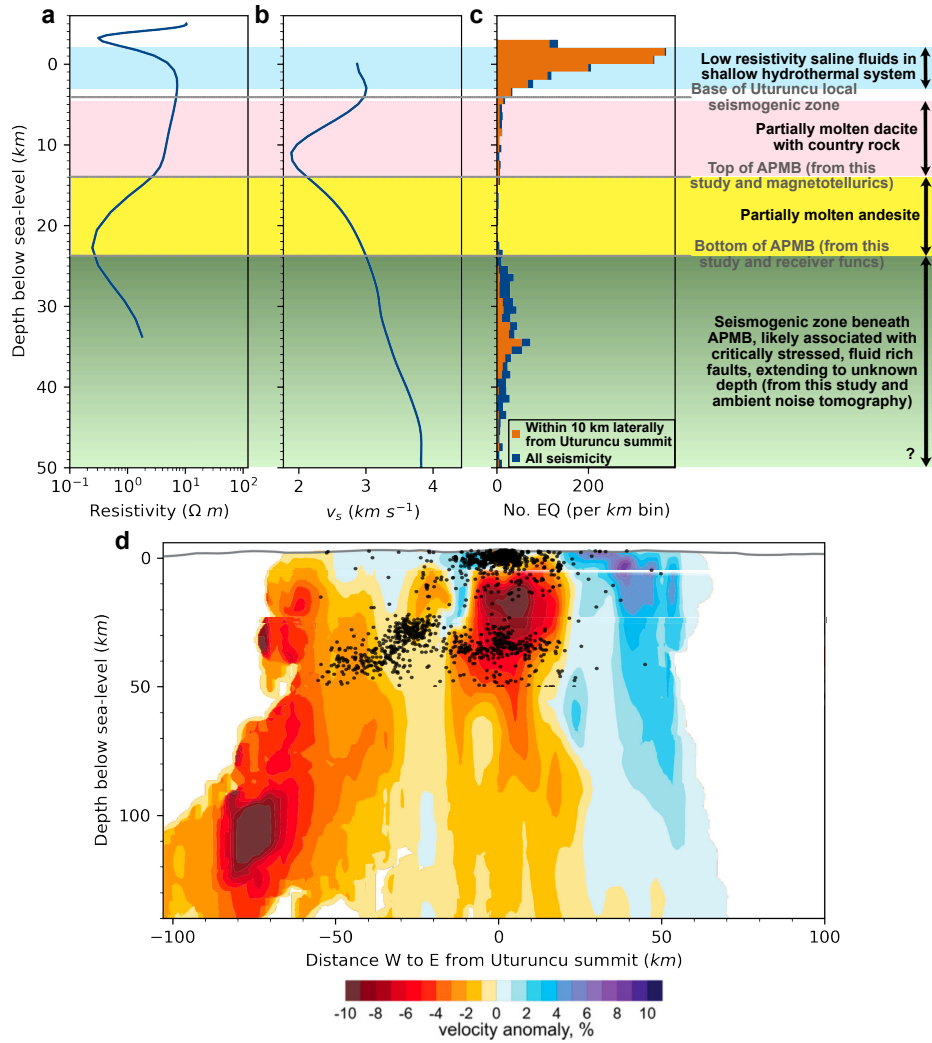


Figure 6 – Schematic summary of the interpretations from the seismicity results presented in this study. Black dots are observed seismicity. Numbered points are referred to in the text.



808

809 *Figure 7 – Summary of how the results of this study compare with observations from previous studies. (a)-(c) Depth profiles*
 810 *of resistivity (Comeau et al., 2016), v_s from ambient noise tomography (Ward et al., 2013), and seismicity binned by depth*
 811 *(from this study). Interpretations shown are based on those presented in Pritchard et al. (2018) (Figure 2) and references*
 812 *therein, along with the new contributions from this study. (d) Plot of S-wave tomography results of Kukarina et al. (2017),*
 813 *overlaid with the seismicity from this study. Note that we only study seismicity detected up to 50 km bsl.*